ADVANCED MATERIALS
www.advmat.de

Fe-Intercalation Dominated Ferromagnetism of van der Waals Fe_3GeTe_2

Yueshen Wu, Yuxiong Hu, Cong Wang, Xiang Zhou, Xiaofei Hou, Wei Xia, Yiwen Zhang, Jinghui Wang, Yifan Ding, Jiadian He, Peng Dong, Song Bao, Jinsheng Wen, Yanfeng Guo, Kenji Watanabe, Takashi Taniguchi, Wei Ji, Zhu-Jun Wang,* and Jun Li**

Fe_3GeTe_2 have proven to be of greatly intrigue. However, the underlying mechanism behind the varying Curie temperature (T_c) values remains a puzzle. This study explores the atomic structure of Fe_3GeTe_2 crystals exhibiting T_c values of 160, 210, and 230 K. The elemental mapping reveals a Fe-intercalation on the interstitial sites within the van der Waals gap of the high-T_c (210 and 230 K) samples, which are observed to have an exchange bias effect by electrical transport measurements, while Fe intercalation or the bias effect is absent in the low-T_c (160 K) samples. First-principles calculations further suggest that the Fe-intercalation layer may be responsible for the local antiferromagnetic coupling that gives rise to the exchange bias effect, and that the interlayer exchange paths greatly contribute to the enhancement of T_c. This discovery of the Fe-intercalation layer elucidates the mechanism behind the hidden antiferromagnetic ordering that underlies the enhancement of T_c in Fe_3GeTe_2.

1. Introduction

The recent discovery of 2D magnets offers a promising opportunity to explore both the fundamental aspects of physics and practical applications, such as spintronic devices. Researchers first observed 2D magnets by exfoliating the bulk crystals of $NiPS_3$,[1,2] $FePS_3$,[3,4] CrI_3,[5–7] $Cr_2Si_2Te_6$,[8] and $Cr_2Ge_2Te_6$.[9] However, as these crystals are semiconductors or insulators, it is impossible to directly evaluate their magnetism using transport measurements or apply them to electronic devices.[10–12] Quantitatively probing the magnetism of monolayer or few-layer crystals is technically challenging. Indirect techniques, such as the low-temperature magneto-optical

Y. Wu, Y. Hu, X. Zhou, X. Hou, W. Xia, Y. Zhang, J. Wang, Y. Ding, J. He, P. Dong, Y. Guo, Z.-J. Wang, J. Li
School of Physical Science and Technology
ShanghaiTech University
Shanghai 201210, China
E-mail: wangzhj3@shanghaitech.edu.cn; lijun3@shanghaitech.edu.cn

C. Wang, W. Ji
Beijing Key Laboratory of Optoelectronic Functional Materials and Micro-Nano Devices, Department of Physics
Renmin University of China
Beijing 100872, China
E-mail: wji@ruc.edu.cn

C. Wang
Key Laboratory of Quantum State Construction and Manipulation (Ministry of Education)
Renmin University of China
Beijing 100872, China

X. Zhou, X. Hou, W. Xia, Y. Zhang, J. Wang, Y. Ding, J. He, P. Dong, Y. Guo
ShanghaiTech Laboratory for Topological Physics
ShanghaiTech University
Shanghai 200031, China

S. Bao, J. Wen
School of Physics & Collaborative Innovation Center of Advanced Microstructures
Nanjing University
Nanjing 210093, China

K. Watanabe
Research Center for Functional Materials
National Institute for Materials Science
1-1 Namiki, Tsukuba 305-0044, Japan

T. Taniguchi
International Center for Materials Nanoarchitectonics
National Institute for Materials Science
1-1 Namiki, Tsukuba 305-0044, Japan

J. Li
State Key Laboratory of Functional Materials for Informatics
Shanghai Institute of Microsystem and Information Technology
Chinese Academy of Sciences
865 Changning Road, Shanghai 200050, China

J. Li
Wuhan National High Magnetic Field Center
Huazhong University of Science & Technology
Wuhan 430074, China

The ORCID identification number(s) for the author(s) of this article can be found under https://doi.org/10.1002/adma.202302568

DOI: 10.1002/adma.202302568

Kerr effect[9,13] or scanning single-spin magnetometer based on diamond nitrogen-vacancy centers,[14] have been applied to address this challenge. The recent observation of 2D ferromagnetic Fe_3GeTe_2 (FGT), thanks to its metallic nature with high carrier density up to 10^{21} cm^{-3}, provides a path to study both the charge and spin degrees of freedom in 2D magnetic systems.[15–17] FGT exhibits a high Curie temperature (T_c) that is representative from 200 K in bulk to 100 K in monolayer crystals.[18,19] The T_c of an N-layer crystal follows an empirical formula as $T_c(N) = [1 - (C/N)^{\lambda}]T_c^{3D}$, where C is a non-universal constant, and $\lambda = 1/\nu$ demonstrates the critical exponent ν of the spin dimensionality in the bulk 3D crystal.[11] However, an ionic gating could significantly enhance the T_c of trilayer crystals up to room temperature.[20] Later experiments demonstrate that ionic gating can also dramatically enhance the coercive field (H_c). [21] Alternatively, the T_c and H_c can be tuned by Fe vacancy.[22] The tunable magnetic properties reinforce the potential application of FGT in electrically controlled magnetoelectronic devices.[23–27]

In the lattice structure of FGT, each unit cell contains two quintuple layers, where Te, Fe, Fe–Ge, Fe, and Te layers are successively stacked. Fe atoms in the Fe and Fe–Ge layers exhibit two inequivalent Fe sites but with different valence, namely, Fe^{3+} (Fe-1 site) and Fe^{2+} (Fe-2 site). Both have partially filled d-orbitals, but they induce considerably different magnetic pictures as local magnetic moment and itinerant ferromagnetic order, respectively.[10–12,15–21,28] Therefore, it is essential to explore the exact atomic structure of both Fe-1 and Fe-2 sites. Chemical doping or occupancy on either site can locally change the magnetic exchange interaction and induce modification of T_c and H_c in a wide range.

In this study, an investigation into the atomic structure of Fe ions was conducted on samples with high-T_c (230 K), intermediate-T_c (210 K), and low-T_c (160 K). The scanning transmission electron microscopy and energy-dispersive X-ray spectroscopy (EDS) techniques were utilized to explore the atomic structure of the FGT crystals with varying T_c. In the high-T_c (230 K) samples, Fe-intercalation was observed on the interstitial sites in the van der Waals gap, while the low-T_c crystals lacked such intercalation. The Hall resistivity loop measurements showed the presence of an exchange bias effect in the high-T_c samples, whereas the low-T_c (160 K) samples exhibited no exchange bias effect. The exchange bias effect can be attributed to the coexistence of ferromagnetic and antiferromagnetic interface (center). To investigate the underlying antiferromagnetic coupling in the inter-layer ferromagnetic system, first-principles calculations were conducted to determine the contribution of the Fe-intercalation layer, which plays a role in local antiferromagnetic coupling for the exchange bias effect. The introduced interlayer exchange paths were found to significantly enhance T_c. The identification of the Fe-intercalation layer provides a means to explore the mechanism behind the enhancement of T_c and H_c of FGT.

2. Results and Discussion

2.1. Structure Analysis

We utilized a transmission electron microscope that is double Cs-corrected and is equipped with energy-dispersive X-ray spectroscopy to accurately reconstruct the lattice structure. The crystals were sectioned by focused ion beam (FIB) along three crystal planes indexed as (001), $(1\bar{2}0)$, and (100), as depicted in the schematic image in Figure S3A–D (Supporting Information). **Figure 1** displays the high-angle annular dark-field images captured using scanning transmission electron microscopy mode (HAADF-STEM) and the corresponding EDS atomic resolution mapping of FGT samples having different T_c values of 160, 210, and 230 K. The HAADF-STEM images are suitable for identifying all ions based on their size and electronic states since the Ge and Te anions are much larger than the Fe cations. Moreover, the HAADF-STEM images are in good agreement with the cartoon of the crystal structure along the $(1\bar{2}0)$ plane, and the planes of (100) and (001) are also consistent with the structure (see Figures S3E–J, Supporting Informationm). Additionally, the Fe-1 and Fe-2 sites are identifiable, where Fe-2 is positioned on the same layer with the Ge ions. Some Fe ions in the van der Waals gap (also see Figure S5, Supporting Information) can be identified, suggesting the Fe intercalation.

2.2. Elementary Distribution Analysis

Elementary mappings obtained through EDS for the intermediate-T_c and high-T_c crystals (Figure 1B,C) indicate the presence of three distinct kinds of defects. First, an additional layer of weaker spots between two Te-sublayers was observed in the Te mapping toward $(1\bar{2}0)$ plane, and such Te ions were also observed along the (100) plane. Based on the lattice cartoon of Ge and Te ions along (100) and $(1\bar{2}0)$ planes, it was found that the substitution of Te occurred on the Ge sites. Second, the Ge mapping demonstrated the doping of a few Ge on the Te sites. Third, a Fe intercalation layer was clearly observed within the van der Waals gap in the Fe mapping toward both $(1\bar{2}0)$ and (100) planes. The HAADF-STEM image also confirmed the presence of such an intercalation layer within the van der Waals gap. However, no occupation of Ge or Te on Fe sites was detected.

In the low-T_c crystal, as shown in Figure 1A, both HAADF-STEM and EDS images demonstrated the absence of Fe-intercalation, while the antisite defects of Ge and Te anions were observed. The antisite of Te and Ge was found in all high-T_c, intermediate-T_c and low-T_c crystals, indicating that it was not the main factor that modulated T_c in different samples. On the other hand, the additional layer of Fe ion not only contributed to the carriers of FGT, but also modified the magnetic coupling, thus inducing peculiar magnetic ordering.

2.3. Density Functional Theory Calculations on the Defects

The application of density functional theory (DFT) was utilized to reveal the underlying cause of Fe intercalation and its effects on the Curie temperature in FGT. The primary origin of intercalated Fe can be attributed to the segregation of Fe ions from their original sites to the interlayer region, resulting in the creation of Fe vacancies at those sites. This process can be facilitated by the presence of additional atoms, such as Te or Ge, that fill these Fe vacancies, leading to the formation of antisite defects. Formation enthalpies of several vacancies, antisite defects, and

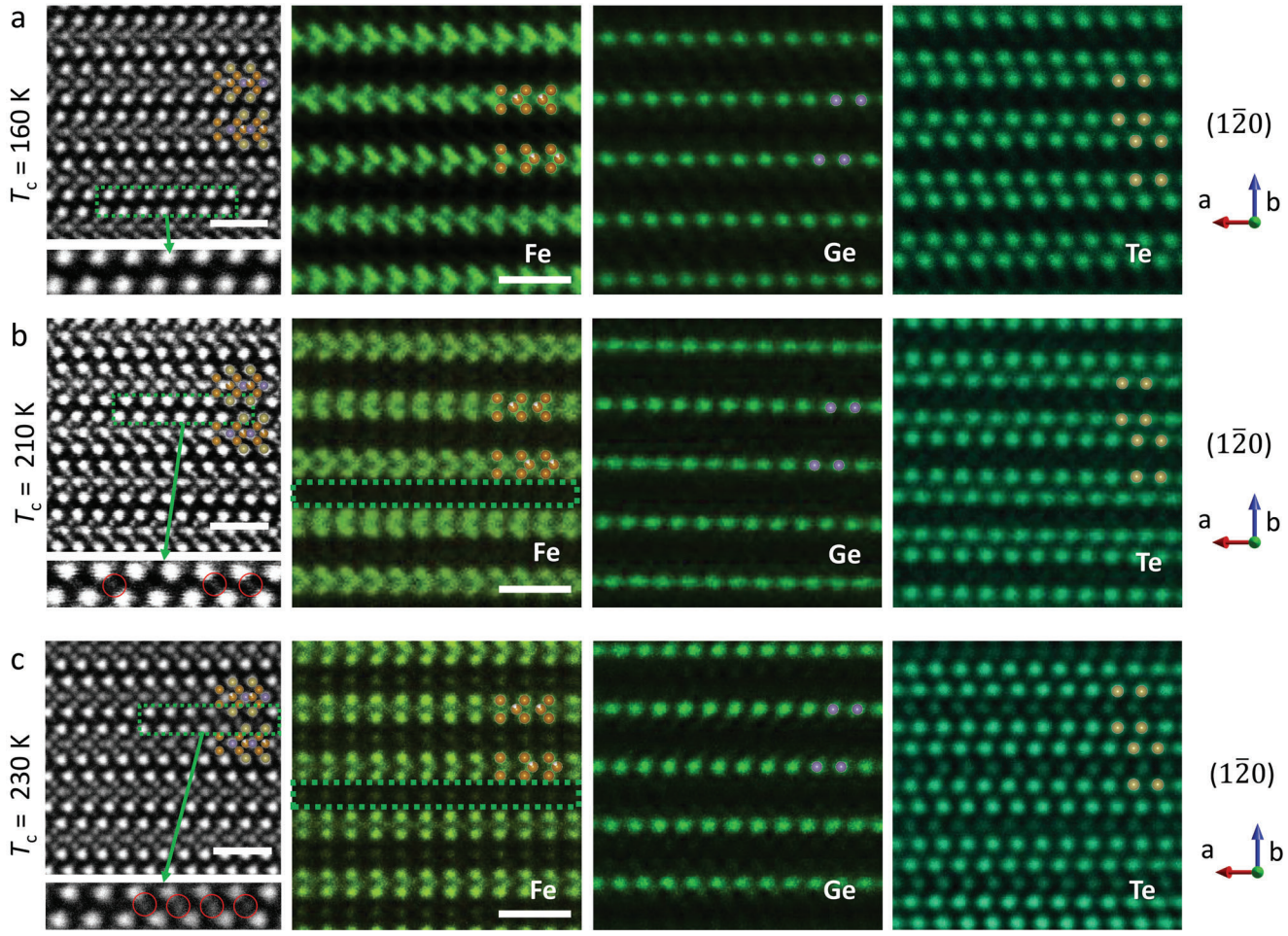

Figure 1. The image shows a Cs-corrected HAADF-STEM image of Fe_3GeTe_2 crystals with EDS mappings of Fe, Te, and Ge atoms toward the (1$\bar{2}$0) plane. The EDS mappings in the image are optimized using both a Wiener filter and a weak Wiener filter. The crystals are labeled (A), (B), and (C), representing low (T_c = 160 K), intermediate (T_c = 210 K), and high (T_c = 230 K) T_c values, respectively. In the image, brown, lilac, and orange balls represent Fe, Ge, and Te atoms, respectively. The green dashed-line frames in the image highlight the van der Waals gap, while the red circle in panels (B) and (C) marks the Fe intercalation. The scale bar in the image is 1 nm.

their various combinations, including Fe^{3+} (V_{Fe3+}), Fe^{2+} (V_{Fe2+}), Ge (V_{Ge}), and Te (V_{Te}) vacancies, Te_{Ge} antisites, bare Fe intercalation ($Fe_{3+x}GeTe_2$), as well as combinations of $Fe_{3+x}GeTe_2$ with Ge_{Fe3+}, Ge_{Fe2+}, Te_{Fe3+}, and Te_{Fe2+} antisites, were examined in our calculations. **Figures 2**A–C and Figure S5 (Supporting Information) illustrate their formation enthalpies as a function of Fe, Ge, and/or Te chemical potentials. V_{Fe2+} (red) and $Fe_{3+x}GeTe_2$ (blue) exhibit the lowest formation enthalpies among all considered defects in Fe deficient and rich limits, respectively, as shown in Figure 2A. Nevertheless, the combination of V_{Fe2+} and $Fe_{3+x}GeTe_2$ (V_{Fe2+} + $Fe_{3+x}GeTe_2$) has a higher formation enthalpy under both Fe deficient and Fe rich limits, indicating that it is less likely to be the source of Fe intercalation. Although this combination can intrinsically introduce intercalated Fe atoms, it requires additional energy gain for stabilization.

A potential method for stabilization involves occupying the Fe vacancy with Ge or Te atoms, resulting in the formation of antisite defects. In the Te-rich regime, the formation enthalpy of the Te/Ge antisite (Te substituting Ge) lies within a range of -0.3 to 2.0 eV (as shown in Figure 2B), which is the most energetically favored among all considered antisite defects. This is consistent with the most frequently observed Te substitution at Ge sites in our experiments (as depicted in Figure 1). The substituted Ge atoms have a propensity to occupy Fe^{3+} sites instead of Fe^{2+} sites, as the filling of the former site (Fe^{3+}) provides an additional energy gain of at least 0.8 eV (as shown in Figure 2C; Figure S6, Supporting Information). Therefore, we may infer that the introduction of intercalated Fe atoms is most likely facilitated by the formation of Te_{Ge} and Ge_{Fe3+} antisite defects in FGT. This process could be regulated, in principle, by controlling the supplying ratio of Te.

Incorporating the Te_{Ge} antisite defect and/or Fe intercalation presents an opportunity to further adjust the magnetic properties and spin exchange couplings of FGT. Upon considering the Te_{Ge} antisite defects, an intralayer and interlayer ferromagnetic (FM) state becomes the most energetically favored magnetic configuration (Figure 2D–G; Figure S7, Supporting Information). This state is more stable by 14 meV/Fe than the antiferromagnetic

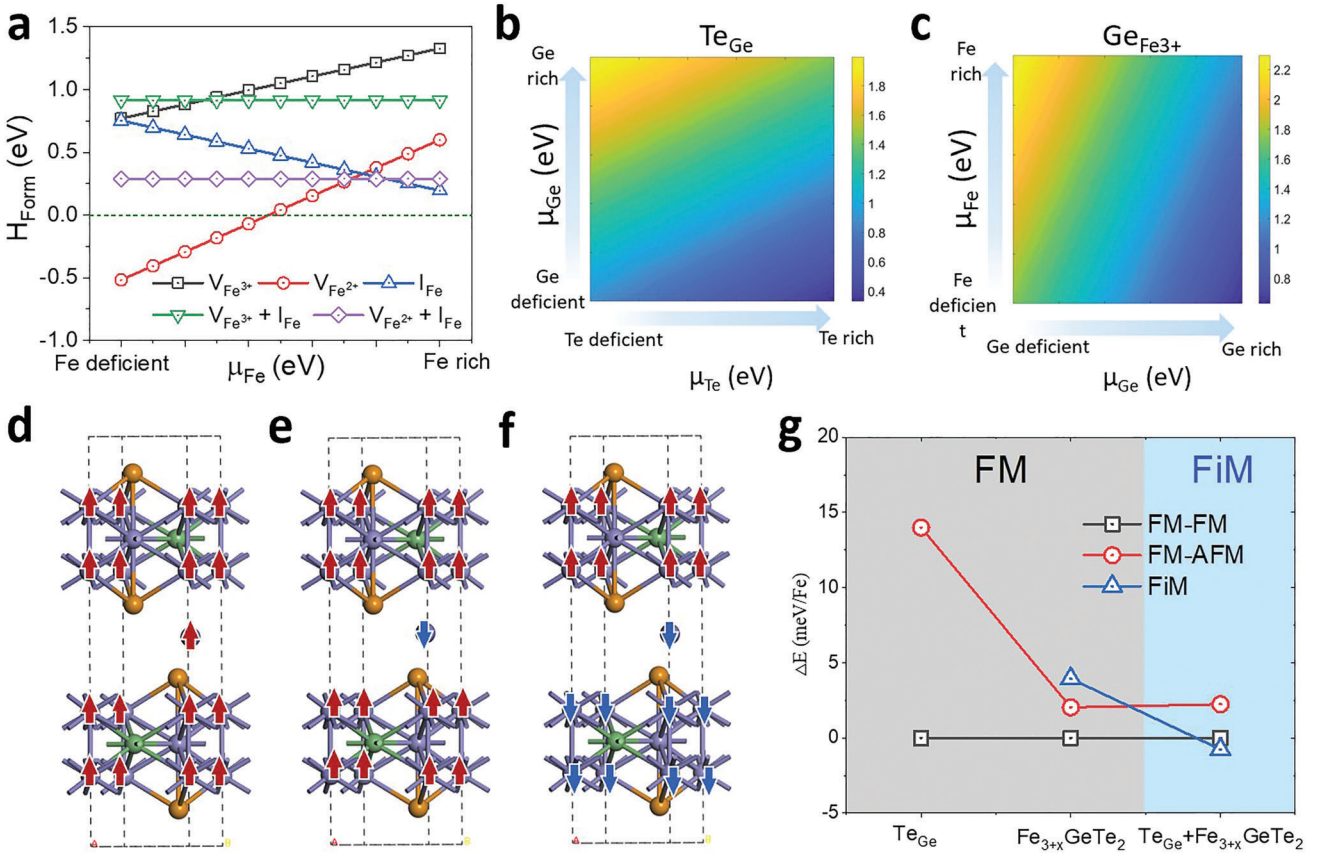

Figure 2. A) Enthalpies of formation for the vacancies V_{Fe2+} and V_{Fe3+} and for Fe intercalations resulting from Fe atoms escaping from vacancies in the Fe^{3+} or Fe^{2+} positions are presented. B,C) Formation enthalpies of the antisite defects Te_{Ge} and Ge_{Fe3+} are provided. D–F) Schematic representations of interlayer magnetic orders, including FM(d), FiM(e), and AFM(f), are depicted. Only Fe atoms are shown here for better presentation. Blue and red balls represent two anti-parallel orientations of magnetic moments on Fe atoms, respectively. g) Relative total energies of the FM (black rectangles), intercalation FiM (blue triangles), and interlayer AFM (red circles) orders of FGT bulk with different types of defects are compared. The reference zero is chosen as the energies of the FM order.

(AFM) order, and is consistent with the observed FM behavior in FGT samples, where Te_{Ge} antisite is commonly present. As illustrated in Figure 2G, the FM state remains the ground state when the intercalated Fe is situated in the interlayer region sandwiched by FGT free of Te_{Ge} antisite defects. However, in the presence of both Te_{Ge} antisite and Fe intercalation, a ferrimagnetic order (FiM, Figure 2E) emerges, where the intercalated Fe sublayers are AFM coupled with adjacent FGT layers, and this configuration is energetically favored. This local AFM coupling can potentially give rise to an exchange bias effect in the high-T_c samples with both Te_{Ge} antisite and Fe intercalation.

2.4. Fe Intercalation Modified Exchange Couplings

Incorporation of Fe intercalation would furnish additional magnetic moments and exchange paths, thus reinforcing magnetic couplings along the interlayer direction in FGT. To assess the tunability of the Curie temperature, we computed the spin-exchange coupling (SEC) parameters based on a Heisenberg model, which are indicated with dashed arrows in different colors in **Figure 3**A and listed in Table S2 (Supporting Information). Monte Carlo simulations were executed with an anisotropic Heisenberg (AH) model (refer to the Methods for elaboration). Local magnetic moments of Fe atoms along the easy magnetization axis, as disclosed by Monte Carlo simulations, were depicted in Figure 3B for FGT with defects. Based on the derived SEC parameters and the easy axis single-ion anisotropy, a T_c value of 148 K was obtained in FGT with Te_{Ge} antisite defects, which is in close proximity to the experimental value of 160 K of low-T_c ferromagnetic samples. As the magnetic couplings within FGT layers are predominantly determined by the intrinsic FGT exchange couplings and Te_{Ge} antisite defects, we further considered a J_7 to describe the spin exchange between the intercalated Fe and the Fe atoms in the adjacent FGT layers. Our calculations demonstrated that the value of J_7 is highly adjustable, ranging from -3.0 to 15.9 meV/Fe, depending on the density of the intercalated Fe atoms (Table S3, Supporting Information). Due to the augmented number of exchange paths and enlarged J_7 value, T_c elevates from 160 to 250 K with an increase in Fe intercalation density (Figure 3B ;Figure S8, Supporting Information), indicating that Fe intercalation is an exceptionally efficient method of enhancing T_c in FGT. It worth noting that including spin-orbit coupling effect only makes quantitatively small change (less than 1 meV/Fe) to the relative total

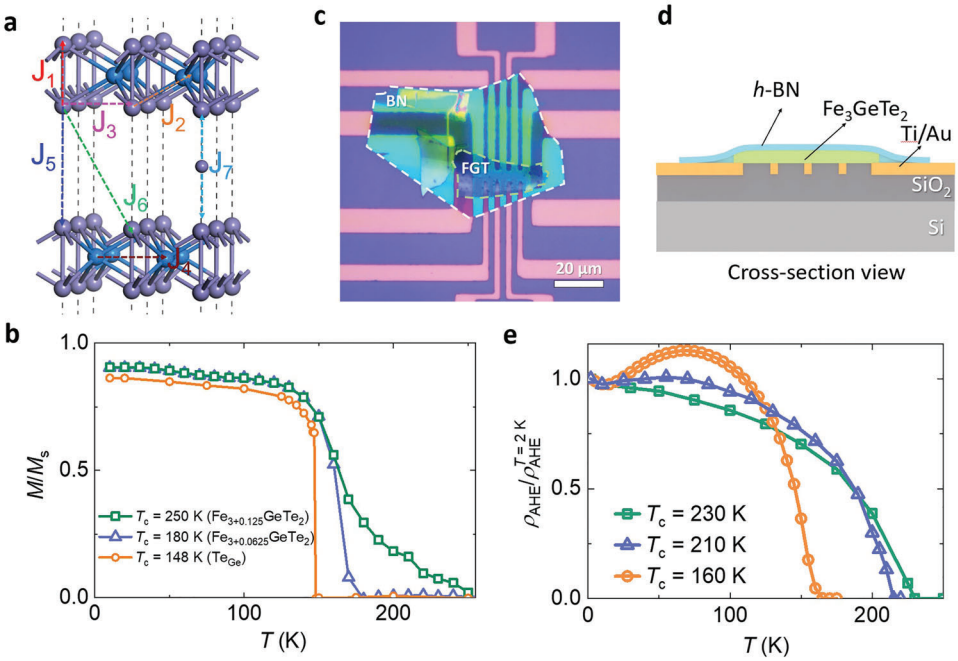

Figure 3. A) A perspective view of FGT is presented, highlighting the SEC parameters between Fe atoms with dashed arrows. For better presentation, only Fe atoms are shown, with slate-blue and blue balls representing Fe^{3+} and Fe^{2+} atoms, respectively. Specifically, J_7 corresponds to the exchange parameter between intercalated Fe and Fe atoms in adjacent FGT layers. B) The on-site magnetic moments are shown as a function of temperature, as revealed by Monte Carlo simulations. The amount of Fe labeled in Figure 3B comes from settings in our DFT calculations. C) An optical image of a typical device with a thickness of 25 nm is presented. A BN slice with a thickness of about 10 nm was covered on top of FGT to prevent oxidation. D) A cross-section view of the device is shown. The Ti/Au electrodes were buried onto the SiO_2/Si substrates so that the FGT and BN slices could be stacked onto a flat substrate, avoiding the collapsing problem that often occurs at the edge steps of the electrodes in a conventional method. E) The anomalous Hall resistance ρ_{AHE} is plotted as a function of temperature, indicating Curie temperatures of 160 K, 210 K, and 230 K, respectively.

energies and does not qualitatively change the calculated magnetic ground states (Table S4, Supporting Information).

The magnetic characteristics of three distinct samples with varying T_c were assessed through measurements of the anomalous Hall effect and magnetic moment. The magnetic field was applied along the c-axis, and the FGT flakes were transferred onto pre-patterned Ti/Au electrodes under an inert atmosphere, as illustrated in Figure 3C,D. The temperature dependent normalized anomalous Hall resistivity (ρ_{AHE}) was determined from the ρ_{AHE}-H curves in Figure S9 (Supporting Information), as shown in Figure 3E. The ρ_{AHE}-T curves approached zero at temperatures of 160 , 210 , and 230 K for the low-T_c, intermediate-T_c, and high-T_c samples, respectively, indicating the same T_c as the bulk crystals. The mangnetic moment measurements in Figure S8 (Supporting Information) also revealed an increasing magnetic moments per f.u. with increasing T_c, consistent with the augmented number of exchange paths with more Fe intercalations.

2.5. Exchange Bias Effect

Our density functional theory (DFT) calculations of FGT, incorporating both TeGe antisite and Fe intercalation, indicate that intercalated Fe atoms could induce local antiferromagnetic (AFM) coupling between intercalated Fe sublayers and adjacent FGT layers, resulting in an exchange bias effect in the high-T_c samples. To investigate this effect, we analyzed the Hall resistance hysteresis loops for both high and low-T_c samples, as shown in Figure S10 (Supporting Information). The low-T_c crystal exhibited a typical anomalous Hall effect (AHE) of ferromagnetism under zero-field-cooling (ZFC), as displayed in Figure S10A (Supporting Information), while the ordinary Hall effect was relatively weak as a flat Hall resistance (R_{xy}) at large magnetic field (H). The coercive fields H_c were almost the same at 160 mT for both positive and negative sweeping directions, comparable to the previous report on FGT.[29] To study the effect of magnetization history on the hysteresis loops, we also examined nine consecutive Hall resistivity loops at 2 K immediately after field-cooling (FC) by applying a magnetic field of 14 T along the c-axis above the T_c (see Figure S10, Supporting Information). The Hall resistance loops of the low-T_c samples were independent of sweeping history or cooling field, and the H_c was fixed at about 160 mT.

In the case of the high-T_c samples, as demonstrated in **Figure 4**A–D and Figure S10E–G (Supporting Information), the hysteresis loops of Hall resistance exhibit a perfectly square shape with no intermediate state, consistent with the Stoner-Wohlfarth model. Notably, the magnetization reversal process is observed to have an asymmetric shape, with the center of the hysteresis loop shifted from zero field by a certain value, resulting in different coercive fields H_{c1} and H_{c2}. This asymmetric R_{xy} hysteresis loop is a typical behavior of the exchange bias effect, which is essentially attributed to the interfacial coupling between a ferromagnetic (FM) layer and an adjacent antiferromagnetic (AFM) layer.[30]

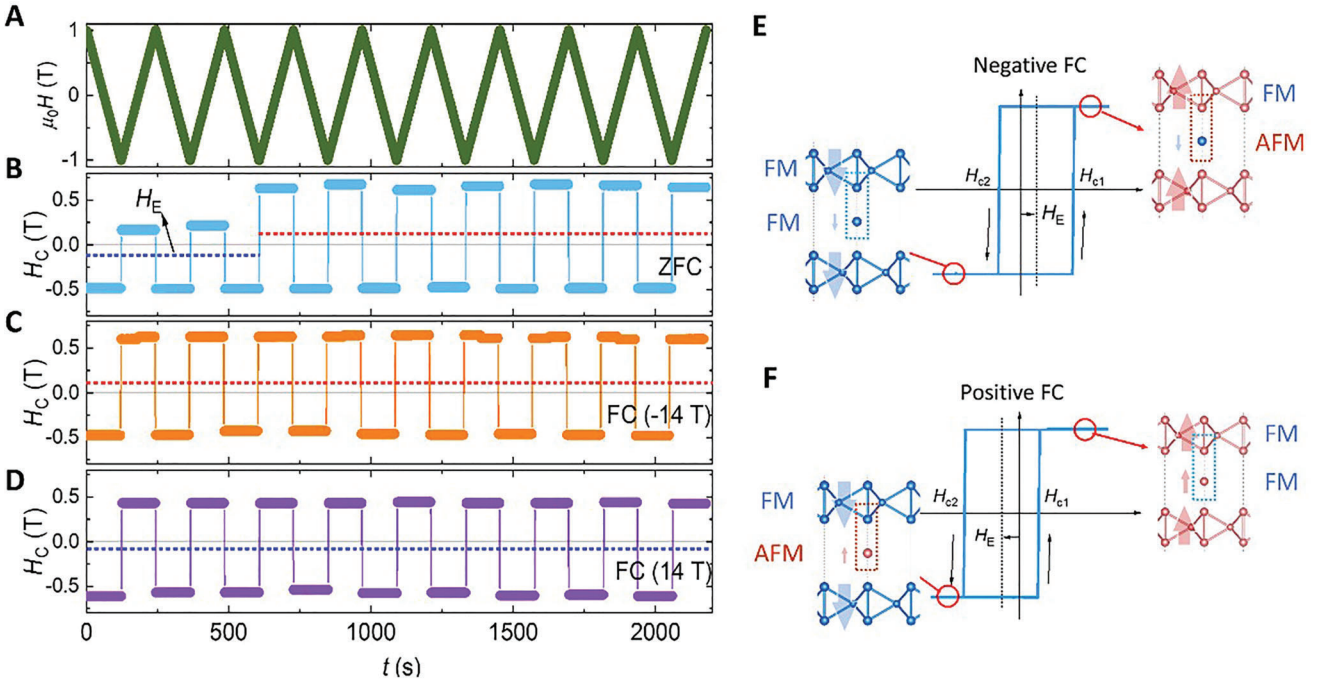

Figure 4. A) Magnetic field sweeping was performed nine times to measure the magnetization loop. B–D) Nine consecutive Hall resistivity loops were measured under three different conditions: zero-field-cooling (ZFC), negative field-cooling FC (-14 T), and positive field-cooling FC (14 T), respectively. The fixed coercive fields at the negative and positive branches are indicated by blue and red dashed lines, and the exchange field responds to the positive or negative field cooling. All Hall resistance loops were measured at a temperature of 2 K. E,F) Schematic images of the magnetization loop of the high-T_c FGT were obtained under negative FC (-14 T) and positive FC (14 T), respectively. The red cycles depict the schematic images of the exchange bias effect induced by the local Fe-intercalation-induced FM/AFM interface. The red and blue arrows represent the magnetic moment up and down on Fe atoms. Under the relatively large FC (14 T), the AFM coupling from local Fe-intercalation has yielded a completely spin-flip transition.

The exchange bias effect exhibited by the high-T_c samples is noteworthy for its FC dependent behavior. When the system is subjected to ZFC, a fixed coercive field is observable on the negative side of H_{c2} for all loops. Conversely, the positive side of H_{c1} fluctuates with sweeping history, leading to a variable HE within a broad range from -162 to 89 mT. The ZFC exchange bias effect is atypical, yet consistent with previous research into gating induced exchange bias effect in FGT.[21] Once exposed to FC of a high magnetic field (±14 T), as illustrated in Figure 4C,D, the exchange bias field displays greater stability than those obtained from ZFC. With a negative field cooling (-14 T), the coercive fields are almost biased to the positive side, whereas applying a positive FC of 14 T causes the coercive fields to shift to the negative side, in line with a negative exchange bias effect. As a result, the exchange field (HE) is primarily fixed at 89 mT for -14 T FC and -72 mT for 14 T FC.

Moreover, the antiferromagnetic (AFM) coupling has the ability to increase the coercive fields of the high-T_c sample to approximately 640 mT, which is significantly higher than that of the low-T_c sample (±160 mT). This intensification of magnetic coupling from the low-T_c crystals is evident in the square-shaped hysteresis loops of Hall resistance and the enhanced H_{c1} of the high-T_c FGT. However, unlike the conventional training effect observed in FM/AFM bilayer systems,[31] there is always a fluctuation of HE, as discussed in detail in Supplementary Materials. Therefore, identifying the relationship between the local atomic structure and the AFM coupling within the FM ordering is crucial to uncover the source of the exchange bias effect.

In essence, it can be concluded that Fe intercalation is responsible for the emergence of the exchange bias effect in the high-T_c samples. In the low-T_c crystal, all magnetic moments at Fe-1 and Fe-2 sites are ferromagnetically coupled, whereas the intercalated Fe may locally induce antiferromagnetic coupling to adjacent layers. The pinning effect of the FM/AFM interface on the FM domain is crucial in achieving the exchange bias effect. It is worth noting that the intercalated Fe is not uniformly filled but randomly distributed at interstitial sites. Thus, the FM/AFM interface is more likely to be the pinning sites. By gradually ramping up the high magnetic fields to 14 T while cooling, the magnetic moment in the AFM component overcomes its exchange energy to align along H, and the AFM coupling at the FM/AFM interface can be well-defined. Consequently, the exchange bias effect is turned from negative to positive, as shown in Figure 4E,F for 14 T and -14 T cooling, respectively. When under ZFC, FM/AFM interfaces (center) can be spontaneously generated after the FM transition, although the polarization is randomly distributed for each interface due to the random formation of the ferromagnetic domain. The polarization direction of the FM domain can be well-aligned under relatively low field sweeping (900 mT), while the AFM can hardly be reoriented. Thus, the pinning effect still exists, resulting in the exchange bias effect.

3. Conclusion

To summarize, we have established a connection between the magnetism and structure of Fe_3GeTe_2 with varying Curie temperature using electrical transport measurements, STEM, and first-principles calculations. Our results demonstrate the presence of an exchange bias effect in high-T_c samples, indicating the existence of a ferromagnetic and antiferromagnetic interface at the center, while this effect is absent in low-T_c samples. Atomic-resolution scanning transmission electron microscopy and energy-dispersive X-ray spectroscopy imaging provide element-resolved atomic structure information of Fe_3GeTe_2 in real-space and confirm the presence of Fe intercalation on interstitial sites in the van der Waals gap in high-T_c samples. First-principles calculations further support the notion that the Fe-intercalation layer can lead to local antiferromagnetic coupling for the exchange bias effect, thus significantly enhancing both antiferromagnetic coupling and T_c. The discovery of the Fe-intercalation layer provides a mechanism for enhancing T_c and H_c in Fe_3GeTe_2, namely, the hidden antiferromagnetic ordering due to the Fe-intercalation. It also offers a path to control T_c and H_c in Fe_3GeTe_2 by manipulating the external magnetic coupling within the inter-layer ferromagnetic system, which is promising for the development of spintronic devices.

4. Experimental Section

Crystal Growth: The bulk crystal of high-T_c and intermediate-T_c FGT was synthesized by the chemical vapor transport (CVT) method. Fe (99.95%, Aldrich), Ge (99.999%, Aladdin) blocks, and Te (99.99%, Aladdin) granules in a molar ratio of 3:1:2 were mixed using a mortar for 20 min. The starting materials were placed into an alumina crucible with iodine. The crucible was sealed into a quartz tube and was subsequently placed in a two-temperature zone tube furnace. For high-T_c sample, one end of the quartz tube loading the mixture was kept at 750 °C and another end for the crystal growth was kept at 600 °C. For intermediate-T_c sample, one end of the quartz tube loading the mixture was kept at 750 °C and another end for the crystal growth was kept at 650 °C. After 150 h, large and thin pieces of black Fe_3GeTe_2 plates with metallic cluster were obtained at the cold end of the tube.

The bulk crystal of low-T_c FGT was synthesized by self-flux method. Fe powder, Ge blocks and Te powder in a molar ratio of 3:3:6 were mixed and placed into an alumina crucible. The crucible was sealed into a quartz tube under a vacuum of 10^{-4} Pa and subsequently heated in a furnace up to 1000 °C in 10 h. After reaction at this temperature for 20 h, the assembly was slowly cooled down to 550 °C at a temperature decreasing rate of 3 °C h_{-1} and stayed at 550 °C for 15 h. The assembly was finally naturally cooled down to room temperature by shutting down the furnace and thin pieces of black crystals were obtained.

The crystal structure was confirmed by single crystal X-ray diffraction (XRD, Bruker D8) and θ-2θ method (Bruker D8). The XRD patterns showed the clear diffraction patterns and lattice parameters agree well with the standard card (see Figures S1 and S2 and Table S1, Supporting Information), guaranteeing the quality of the crystal. The stoichiometry of these crystals were measured by inductively coupled plasma optical emission spectroscopy (ICP - OES).

Structure Analysis: The double Cs-corrected scanning transmission electron microscopy (STEM, Grand JEM-ARM300F) was applied to analyze the atomic structure, the microscopy was equipped with a cold field-emission gun and operated at the accelerating voltage of 300 kV. To confirm the exact type of the defects, it cut the crystal by a focused ion beam (FIB, Grand JIB-4700F) along three crystal planes with the index of (001), ($1\bar{2}0$), and (100) as illustrated in Figure S3 (Supporting Information). Here, the thickness of the thin specimens was around 50–100 nm. The energy-dispersive X-ray spectroscopy (EDS) mapping was applied for the element distribution study.

Transport Measurement: For transport measurements, a thin FGT flake was transferred on pre-patterned Ti/Au electrodes under inert atmosphere in Figure 3C,D, using standard mechanical exfoliation and polymer transfer method. The device was wire bonded on the puck and loaded into Physical Property Measurement System (PPMS, Quantum Design) as soon as possible. AHE was measured by Keithley 2400 and 2182A as the current source and voltage meter. A low current of 10 μA was applied to prevent from local heating and current driven effect. The noise level of the system was lower than 600 nV (Figure S17, Supporting Information). The thickness of the FGT was measured by atomic force microscopy and the corresponding color code after the transport measurement. The thicknesses of the measured samples were from 25 to 50 nm.

DFT Calculations: This study performed density functional theory calculations using the same methods described in its previous publications,[32–35] was utilized to reveal the underlying cause of Fe intercalation and its effects on the Curie temperature in FGT. In brief, it used a van der Waals density functional (vdW-DF) method,[36,37] with the optB86b functional for the exchange part (optB86b-vdW[38]), to optimize atomic structures of bulk FGT. The choice of optB86b-vdW usually enables us to well reproduce experimentally measured structure-related properties of 2D materials.[39,40] Given fully relaxed atomic structures, it employed the standard Perdew-Burke-Ernzerhof (PBE) functional,[41] with a proper on-site Coulomb interaction value (PBE+U), to compare energy differences of all considered magnetic configurations. This scheme was found to be capable of revealing magnetic properties highly comparable with those of the Heyd-Scuseria-Ernzerhof (HSE06) functional[42] in 2D magnetic layers, e.g., CrI_3[32] and CrSCl.[43] On-site Coulomb interactions on Fe 3*d* orbitals were considered with two different pairs of *U* and *J* values, namely $U = 3.6$ eV and $J = 0.2$ eV for Fe^{3+} and $U = 4.6$ eV and $J = 1.0$ eV for Fe^{2+}, as revealed by a linear response method.[44] A uniform Monkhorst-Pack k-mesh of 15× 15× 3 was adopted for integrating over the Brillouin zone of a FGT unit cell. An orthorhombic $4 \times 2\sqrt{3} \times 2$ magnetic supercell was used for predicting magnetic properties of FGT bulk crystals with low defect density, in which a MP *k*-mesh of $4 \times 6 \times 1$ was used. A kinetic energy cutoff of 400 eV for the plane-wave basis set was used for both structural relaxations and electronic structure calculations of defective FGT bulk crystals. All atoms could relax until the residual force per atom was less than 0.01 eVÅ^{-1}. Metropolis Monte Carlo simulations were carried out to predict Curie temperatures. A 2D anisotropic Heisenberg model containing both the easy axis single ion anisotropy and the isotropic exchange was adopted with a 50×50 lattice and the periodic boundary condition.

Supporting Information

Supporting Information is available from the Wiley Online Library or from the author.

Acknowledgements

This research was supported in part by the Ministry of Science and Technology (MOST) of China (no. 2018YFE0202700, 2022YFA1603903), the National Natural Science Foundation of China (Grants no. 12004251, 12027804, 11974422, 12104302, 12104303, 61761166009, 11974422, and 12104504), the Fundamental Research Funds for the Central Universities and the Research Funds of Renmin University of China (no. 22XNKJ30), the Natural Science Foundation of Shanghai (Grant no. 20ZR1436100), the Science and Technology Commission of the Shanghai Municipality (21JC1405100), the Strategic Priority Research Program (Chinese Academy of Sciences, CAS) (no. XDB30000000), the start-up funding from ShanghaiTech University, and Beijing National Laboratory for Condensed Matter Physics, the Interdisciplinary Program of Wuhan National High Magnetic Field Center (WHMFC202124). Growth of hexagonal

boron nitride crystals was supported by JSPS KAKENHI (Grant Numbers 19H05790, 20H00354, and 21H05233) and A3 Foresight by JSPS. C.W. was supported by the China Postdoctoral Science Foundation (2021M693479). Calculations were performed at the Physics Lab of High-Performance Computing of Renmin University of China, Shanghai Supercomputer Center. The authors thank the support from Analytical Instrumentation Center (# SPST-AIC10112914), the Electron Microscopy Center and Soft Matter Nanofabrication Laboratory, SPST, ShanghaiTech University.

Conflict of Interest

The authors declare no conflict of interest.

Author Contributions

Y.W., Y.H., C.W., X.Z. contributed equally to this work. Y.W. and J.L. conceived the experiment. Y.W. and X.Z. carried out transport measurements. X.H., W.X., Y.G., S.B., and J.W. grew the crystals. Y.H. and Z.-J.W. carried out the TEM characterization. C.W. and W.J. performed theoretical calculations. J.W., Z.-J.W., and J.L. performed the analysis and interpretation of the data. K.W. and T.T. provided high quality h-BN bulk crystals. All authors assisted in the interpretation of data and contributed to the writing of the manuscript.

Data Availability Statement

The data that support the findings of this study are available from the corresponding author upon reasonable request.

Keywords

2D materials, exchange bias, ferromagnetism

Received: March 20, 2023
Revised: May 25, 2023
Published online: July 21, 2023

[1] C.-T. Kuo, M. Neumann, K. Balamurugan, H. J. Park, S. Kang, H. W. Shiu, J. H. Kang, B. H. Hong, M. Han, T. W. Noh, J.-G. Park, *Sci. Rep.* **2016**, *6*, 20904.
[2] S. Kang, K. Kim, B. H. Kim, J. Kim, K. I. Sim, J.-U. Lee, S. Lee, K. Park, S. Yun, T. Kim, A. Nag, A. Walters, M. Garcia-Fernandez, J. Li, L. Chapon, K.-J. Zhou, Y.-W. Son, J. H. Kim, H. Cheong, J.-G. Park, *Nature* **2020**, *583*, 785.
[3] K.-z. Du, X.-z. Wang, Y. Liu, P. Hu, M. I. B. Utama, C. K. Gan, Q. Xiong, C. Kloc, *ACS Nano* **2016**, *10*, 1738.
[4] J.-U. Lee, S. Lee, J. H. Ryoo, S. Kang, T. Y. Kim, P. Kim, C.-H. Park, J.-G. Park, H. Cheong, *Nano Lett.* **2016**, *16*, 7433.
[5] B. Huang, G. Clark, D. R. Klein, D. MacNeill, E. Navarro-Moratalla, K. L. Seyler, N. Wilson, M. A. McGuire, D. H. Cobden, D. Xiao, W. Yao, P. Jarillo-Herrero, X. Xu, *Nat. Nanotechnol.* **2018**, *13*, 544.
[6] S. Jiang, L. Li, Z. Wang, K. F. Mak, J. Shan, *Nat. Nanotechnol.* **2018**, *13*, 549.
[7] Z. Sun, Y. Yi, T. Song, G. Clark, B. Huang, Y. Shan, S. Wu, D. Huang, C. Gao, Z. Chen, M. McGuire, T. Cao, D. Xiao, W.-T. Liu, W. Yao, X. Xu, S. Wu, *Nature* **2019**, *572*, 497.
[8] M.-W. Lin, H. L. Zhuang, J. Yan, T. Z. Ward, A. A. Puretzky, C. M. Rouleau, Z. Gai, L. Liang, V. Meunier, B. G. Sumpter, P. Ganesh, P. R. C. Kent, D. B. Geohegan, D. G. Mandrus, K. Xiao, *J. Mater. Chem. C* **2016**, *4*, 315.
[9] C. Gong, L. Li, Z. Li, H. Ji, A. Stern, Y. Xia, T. Cao, W. Bao, C. Wang, Y. Wang, Z. Q. Qiu, R. J. Cava, S. G. Louie, J. Xia, X. Zhang, *Nature* **2017**, *546*, 265.
[10] K. S. Burch, *Nat. Nanotechnol.* **2018**, *13*, 532.
[11] M. Gibertini, M. Koperski, A. F. Morpurgo, K. S. Novoselov, *Nat. Nanotechnol.* **2019**, *14*, 408.
[12] B. Huang, M. A. McGuire, A. F. May, D. Xiao, P. Jarillo-Herrero, X. Xu, *Nat. Mater.* **2020**, *19*, 1276.
[13] B. Huang, G. Clark, E. Navarro-Moratalla, D. R. Klein, R. Cheng, K. L. Seyler, D. Zhong, E. Schmidgall, M. A. McGuire, D. H. Cobden, W. Yao, D. Xiao, P. Jarillo-Herrero, X. Xu, *Nature* **2017**, *546*, 270.
[14] L. Thiel, Z. Wang, M. A. Tschudin, D. Rohner, I. Gutiérrez-Lezama, N. Ubrig, M. Gibertini, E. Giannini, A. F. Morpurgo, P. Maletinsky, *Science* **2019**, *364*, 973.
[15] H.-J. Deiseroth, K. Aleksandrov, C. Reiner, L. Kienle, R. K. Kremer, *Eur. J. Inorg. Chem.* **2006**, *2006*, 1561.
[16] H. L. Zhuang, P. R. C. Kent, R. G. Hennig, *Phys. Rev. B* **2016**, *93*, 134407.
[17] Y. Zhang, H. Lu, X. Zhu, S. Tan, W. Feng, Q. Liu, W. Zhang, Q. Chen, Y. Liu, X. Luo, D. Xie, L. Luo, Z. Zhang, X. Lai, *Sci. Adv.* **2018**, *4*, eaao6791.
[18] Z. Fei, B. Huang, P. Malinowski, W. Wang, T. Song, J. Sanchez, W. Yao, D. Xiao, X. Zhu, A. F. May, W. Wu, D. H. Cobden, J.-H. Chu, X. Xu, *Nat. Mater.* **2018**, *17*, 778.
[19] C. Tan, J. Lee, S.-G. Jung, T. Park, S. Albarakati, J. Partridge, M. R. Field, D. G. McCulloch, L. Wang, C. Lee, *Nat. Commun.* **2018**, *9*, 1554.
[20] Y. Deng, Y. Yu, Y. Song, J. Zhang, N. Z. Wang, Z. Sun, Y. Yi, Y. Z. Wu, S. Wu, J. Zhu, J. Wang, X. H. Chen, Y. Zhang, *Nature* **2018**, *563*, 94.
[21] G. Zheng, W.-Q. Xie, S. Albarakati, M. Algarni, C. Tan, Y. Wang, J. Peng, J. Partridge, L. Farrar, J. Yi, Y. Xiong, M. Tian, Y.-J. Zhao, L. Wang, *Phys. Rev. Lett.* **2020**, *125*, 047202.
[22] A. F. May, S. Calder, C. Cantoni, H. Cao, M. A. McGuire, *Phys. Rev. B* **2016**, *93*, 014411.
[23] y. Johansen, V. Risinggard, A. Sudbø, J. Linder, A. Brataas, *Phys. Rev. Lett.* **2019**, *122*, 217203.
[24] K. Zhang, S. Han, Y. Lee, M. J. Coak, J. Kim, I. Hwang, S. Son, J. Shin, M. Lim, D. Jo, K. Kim, D. Kim, H.-W. Lee, J.-G. Park, *Adv. Mater.* **2021**, *33*, 2004110.
[25] X. Wang, J. Tang, X. Xia, C. He, J. Zhang, Y. Liu, C. Wan, C. Fang, C. Guo, W. Yang, Y. Guang, X. Zhang, H. Xu, J. Wei, M. Liao, X. Lu, J. Feng, X. Li, Y. Peng, H. Wei, R. Yang, D. Shi, X. Zhang, Z. Han, Z. Zhang, G. Zhang, G. Yu, X. Han, *Sci. Adv.* **2019**, *5*, eaaw8904.
[26] I. Shin, W. J. Cho, E.-S. An, S. Park, H.-W. Jeong, S. Jang, W. J. Baek, S. Y. Park, D.-H. Yang, J. H. Seo, G.-Y. Kim, M. N. Ali, S.-Y. Choi, H.-W. Lee, J. S. Kim, S. D. Kim, G.-H. Lee, *Adv. Mater.* **2022**, *34*, 2101730.
[27] S. Albarakati, C. Tan, Z.-J. Chen, J. G. Partridge, G. Zheng, L. Farrar, E. L. H. Mayes, M. R. Field, C. Lee, Y. Wang, Y. Xiong, M. Tian, F. Xiang, A. R. Hamilton, O. A. Tretiakov, D. Culcer, Y.-J. Zhao, L. Wang, *Sci. Adv.* **2019**, *5*, eaaw0409.
[28] S. Jiang, J. Shan, K. F. Mak, *Nature Materials* **2018**, *17*, 406.
[29] S. Y. Park, D. S. Kim, Y. Liu, J. Hwang, Y. Kim, W. Kim, J.-Y. Kim, C. Petrovic, C. Hwang, S.-K. Mo, H.-j. Kim, B.-C. Min, H. C. Koo, J. Chang, C. Jang, J. W. Choi, H. Ryu, *Nano Lett.* **2020**, *20*, 95.
[30] J. Nogués, I. K. Schuller, *J. Magn. Magn. Mater.* **1999**, *192*, 203.
[31] R. Zhu, W. Zhang, W. Shen, P. K. J. Wong, Q. Wang, Q. Liang, Z. Tian, Y. Zhai, C.-w. Qiu, A. T. S. Wee, *Nano Lett.* **2020**, *20*, 5030.
[32] P. Jiang, C. Wang, D. Chen, Z. Zhong, Z. Yuan, Z.-Y. Lu, W. Ji, *Phys. Rev. B* **2019**, *99*, 144401.
[33] C. Wang, X. Zhou, Y. Pan, J. Qiao, X. Kong, C.-C. Kaun, W. Ji, *Phys. Rev. B* **2018**, *97*, 245409.
[34] Y. Wang, C. Wang, S.-J. Liang, Z. Ma, K. Xu, X. Liu, L. Zhang, A. S. Admasu, S.-W. Cheong, L. Wang, M. Chen, Z. Liu, B. Cheng, W. Ji, F. Miao, *Adv. Mater.* **2020**, *32*, 2004533.
[35] C. Wang, X. Zhou, L. Zhou, Y. Pan, Z.-Y. Lu, X. Wan, X. Wang, W. Ji, *Phys. Rev. B* **2020**, *102*, 020402.

[36] M. Dion, H. Rydberg, E. Schröder, D. C. Langreth, B. I. Lundqvist, *Phys. Rev. Lett.* **2004**, *92*, 246401.
[37] K. Lee, a. D. Murray, L. Kong, B. I. Lundqvist, D. C. Langreth, *Phys. Rev. B* **2010**, *82*, 081101.
[38] J. Klimeš, D. R. Bowler, A. Michaelides, *Phys. Rev. B* **2011**, *83*, 195131.
[39] Z.-X. Hu, X. Kong, J. Qiao, B. Normand, W. Ji, *Nanoscale* **2016**, *8*, 2740.
[40] J. Qiao, Y. Pan, F. Yang, C. Wang, Y. Chai, W. Ji, *Sci. Bull.* **2018**, *63*, 159.
[41] J. P. Perdew, K. Burke, M. Ernzerhof, *Phys. Rev. Lett.* **1996**, *77*, 3865.
[42] J. Heyd, G. E. Scuseria, M. Ernzerhof, *J. Chem. Phys.* **2003**, *118*, 8207.
[43] C. Wang, X. Zhou, L. Zhou, N.-H. Tong, Z.-Y. Lu, W. Ji, *Sci. Bull.* **2019**, *64*, 293.
[44] M. Cococcioni, S. de Gironcoli, *Phys. Rev. B* **2005**, *71*, 035105.